

Hollow calcite crystals with complex morphologies formed from amorphous precursors and regulated by surfactant micellar structures†

Junwu Xiao and Shihe Yang*

Received 3rd March 2010, Accepted 5th May 2010

DOI: 10.1039/c003839c

Organisms can control the shapes and sizes of inorganic nanocrystals and arrange them into ordered structures such as amorphous precursors, which perform remarkable mechanical and optical functions. This interesting phenomenon has galvanized many attempts to mimic the biomineralization process for synthesizing novel materials. In this work, we study the crystallization processes starting from an amorphous calcium carbonate precursor stabilized by citric acid molecules. By varying cetyltrimethyl ammonium bromide (CTAB) concentrations, we found that the crystallization, in contrast to the classical crystallization, starts from amorphous particles in much the same way as in biomineralization. Novel morphologies of calcium carbonate polycrystals, including hollow radiating cluster-like particles, hollow sheaf-like crystals, and hollow rods, have been identified and found to be regulated by CTAB micellar structures. The mineralization process is discussed in terms of cooperative reorganization of coupled inorganic and organic components, which is relevant to models of matrix-mediated nucleation in biomineralization. The result should help to understand aggregation driven formation of complex material structures as well as biomineralization mechanisms.

Introduction

Biominerals are well-known hybrid materials of hard inorganic and soft organic components in the form of fascinating shapes and highly ordered structures, which widely exist in nature as, for example, bones, teeth, shells, corals and magnetic crystals in bacteria.¹ The remarkable mechanical and optical properties of these materials are generally related to a high level of control over structure, size, morphology, orientation and assembly of the constituents.^{2,3} Therefore, learning from nature on how to synthesize hybrid inorganic–organic materials with specific size, shape, orientation, organization, complex form and hierarchy has been a focus of ongoing interest because of the importance and the potential to design new materials and devices in various fields such as catalysis, medicine, electronics, ceramics, pigments and cosmetics.^{4–12}

Calcium carbonate, one of the most abundant biominerals in organisms and an important industrial raw material in ceramics, paper-making, cosmetics, pigments, rubber industry, *etc.*, has been intensively researched. As the research is intensified on biomineralization mechanisms and bio-inspired mineralization processes,^{13–18} indications are accruing that crystallization does not necessarily proceed along the classical crystallization pathway by attachment of ions/molecules to a primary particle forming a single crystal, but rather follow non-classical crystallization pathways,¹³ *e.g.*, by mesoscopic transformation *via* self-assembly or from metastable or amorphous precursor particles.

To elucidate the mineralization mechanisms involved, researchers have spent efforts to control the formation of oriented CaCO₃ crystals *in vitro*. For example, template-directed CaCO₃ mineralization has been studied *in vitro* by using two-dimensional (2D) molecular assemblies as templates.^{15,19,20} Although the mechanism of crystallization under 2D molecular assemblies has transpired,²¹ the genuine control over crystallization has been elusive in the sense that the calcium carbonate crystals finally formed are always the conventional rhombohedral calcite, dictated by the internal symmetry of the calcite crystal lattice.^{19,20} On the other hand, with the templates of biopolymers,^{22–26} double hydrophilic block copolymers,^{27–29} polyelectrolytes,^{30–33} dendrimers,^{34,35} foldamers,³⁶ *etc.* in bulk phase, unusual complex structures of calcium carbonate crystals have been obtained. It is a fascinating fact that biology yields single crystals whose morphologies bear no relation to their crystallographic structure, such as the skeletal plates of echinoderms, or curved and rounded surfaces in sponge spicules.¹ Thus, it dawns on us that crystallization in the bulk phase of an organic matrix should more realistically realize the kind of morphological control when compared with 2D molecular assemblies. Another interesting finding is that the outcome of crystallization depends dramatically on how the reagents are supplied even when the same surfactant is used. For example, in the presence of cetyltrimethyl ammonium bromide (CTAB), conventional rhombohedral calcite crystals were obtained *via* direct mixing of Ca²⁺ and CO₃^{2–},^{37–39} whereas decomposition of dimethyl carbonate in a Ca²⁺ solution yielded laminated hexagonal vaterite mesocrystals.⁴⁰

Herein, we investigate a different approach to the mineralization of calcium carbonate crystals in an organic matrix of CTAB by starting from a mother solution containing amorphous calcium carbonate (ACC) stabilized by citric acid in bulk phase. This approach bypasses the critical dependence of crystallization

Department of Chemistry, William Mong Institute of Nano Science and Technology, The Hong Kong University of Science and Technology, Clear Water Bay, Kowloon, Hong Kong. E-mail: chsyang@ust.hk

† Electronic supplementary information (ESI) available: Additional SEM images, XRD patterns and EDX profiles of some calcium carbonate product samples. pH drift assay *vs.* reaction time at various CTAB concentrations. See DOI: 10.1039/c003839c

from solutions of Ca^{2+} and CO_3^{2-} on the mode of reagent supply and allows to control crystallite morphologies regardless of their lattice structures, which is reminiscent of the non-classical crystallization found in organisms whereby amorphous phase is, for example, stabilized by acidic glycoproteins and triggered by echinoderms to crystallize in mineralizing compartments.^{41,42}

Experimental

Calcium chloride dehydrate ($\text{CaCl}_2 \cdot 2\text{H}_2\text{O}$), citric acid ($\text{C}_6\text{H}_8\text{O}_7$), sodium carbonate (Na_2CO_3), and cetyltrimethyl ammonium bromide ($\text{C}_{19}\text{H}_{42}\text{BrN}$, CTAB) were used as received without further purification. The crystallization process of calcium carbonate was carried out as follows. Citric acid and calcium chloride were dissolved in deionized water to form 40 mL solution containing CaCl_2 (20 mM) and citric acid (20 mM), followed by addition of sodium carbonate with stirring to form a transparent solution containing 20 mM sodium carbonate. Afterwards, the beaker containing the resulting solution ($\text{pH} \sim 4.5$) was covered with parafilm, which was punched with a needle to form a few holes and then placed in a desiccator. A culture dish containing ~ 1.0 g of ammonium bicarbonate was similarly covered with parafilm, punched with needle holes, and placed on the bottom of the desiccator. After 4.5 h of reaction, the solution was taken out of the desiccator as it just became turbid at a pH of ~ 9.4 . Then, a certain amount of CTAB was added into the above solution with stirring at room temperature. After different periods of reaction from this onward, the precipitates were rinsed with doubly distilled water and ethanol and dried at 40°C for 24 h.

The morphologies were directly examined by scanning electron microscopy (SEM) using JEOL JSM-6700F at an accelerating voltage of 5 kV. Transmission electron microscopy (TEM) observations were carried out on a JEOL 2010 microscope operating at 200 kV. X-ray diffraction (XRD) analyses were performed on a Philips PW-1830 X-ray diffractometer with $\text{CuK}\alpha$ irradiation ($\lambda = 1.5406 \text{ \AA}$). The zeta potential was measured by Zeta Potential Analyzer (Brookhaven Instruments Corporation). Fourier transform infrared spectroscopy (FTIR) analysis was carried out with KBr discs in the region of $4000\text{--}400 \text{ cm}^{-1}$ on Perkin Elmer (Spectrum one). Thermogravimetric analysis (TGA) was performed on TGA Q5000. The heating rate was $10^\circ\text{C min}^{-1}$, under an air flow of 20 mL min^{-1} from $30\text{--}1000^\circ\text{C}$.

Results and discussion

We adopted a standard procedure for calcium carbonate mineralization studies, which is based on the slow supply of CO_2 and NH_3 . This approach can easily control the crystallization process by varying the storage time of a mother solution together with ammonium bicarbonate in a closed container. In the present work, the mother solution contained ACC precursor particles stabilized by citric acid. After mixing the citric acid stabilized ACC and CTAB, the crystallization processes of calcium carbonate were monitored. SEM images of the products formed after 9 h of reaction at various concentrations of CTAB are shown in Fig. 1. When the CTAB concentration was 1 mM, cluster-like crystals were developed from a common core

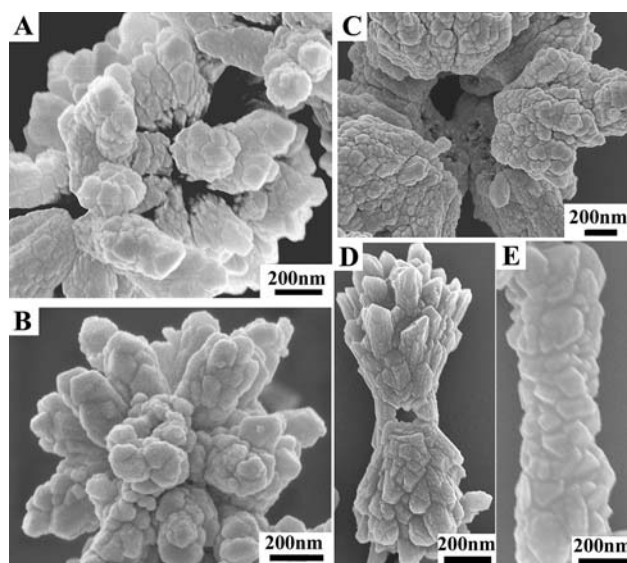


Fig. 1 SEM images of the samples obtained at various concentrations of CTAB after 9 h of reaction: (A) 1 mM, (B) 5 mM, (C) 10 mM, (D) 100 mM and (E) 277 mM.

radiating in all directions with a structure similar to a flower (Fig. 1A). Such a flower morphology was maintained when the CTAB concentration was increased to 5 (Fig. 1B) and 10 mM (Fig. 1C). However, with 10 mM of CTAB, the cores of the particles were empty and the radiating cluster-like crystals became hollow (Fig. 1C), which is more clearly seen from the high magnification SEM image shown in the ESI, Fig. SI-1A.† A further increase in the CTAB concentration to 100 mM promoted more anisotropic growth, yielding hollow calcium carbonate crystals with a sheaf-like morphology (Fig. 1D). Finally, when the CTAB concentration reached 277 mM, rod-shaped crystals but with a rough surface were formed (Fig. 1E), which again bear a hollow structure as can be clearly seen from the SEM image of a ruptured sample (ESI, Fig. SI-1B).† The corresponding XRD patterns reveal that all the samples formed in the presence of CTAB were in the thermodynamically most stable calcite phase (see ESI, Fig. SI-1C).† Furthermore, it is important to notice that the conventional rhombohedral calcite crystals were obtained after 9 h of reaction only when CTAB was absent (ESI, Fig. SI-1D).† On the other hand, previous work has shown that the morphology and polymorph of CaCO_3 crystals formed in the presence of only CTAB or only citric acid or neither are generally similar.^{38,43} Thus, we have established that citric acid and CTAB cooperatively play key roles in the crystallization of calcium carbonate with such complex morphologies ranging from hollow radiating cluster-like particles, hollow sheaf-like crystals, to hollow rods.

To reveal the compositions of the products formed at various CTAB concentrations after 9 h of reaction, we conducted IR spectroscopy and TGA analysis, and the results are presented in Fig. 2. The IR peaks at 874 and 713 cm^{-1} are typical of calcite phase (Fig. 2A),⁴⁴ in accordance with the XRD results. The asymmetric stretching vibration of carbonate ions in the calcite crystals is epitomized by the strong and broad peak at 1450 cm^{-1} . The small peak at 1630 cm^{-1} is associated with the C=O stretching vibration of carboxylate ion derived from citric acid.

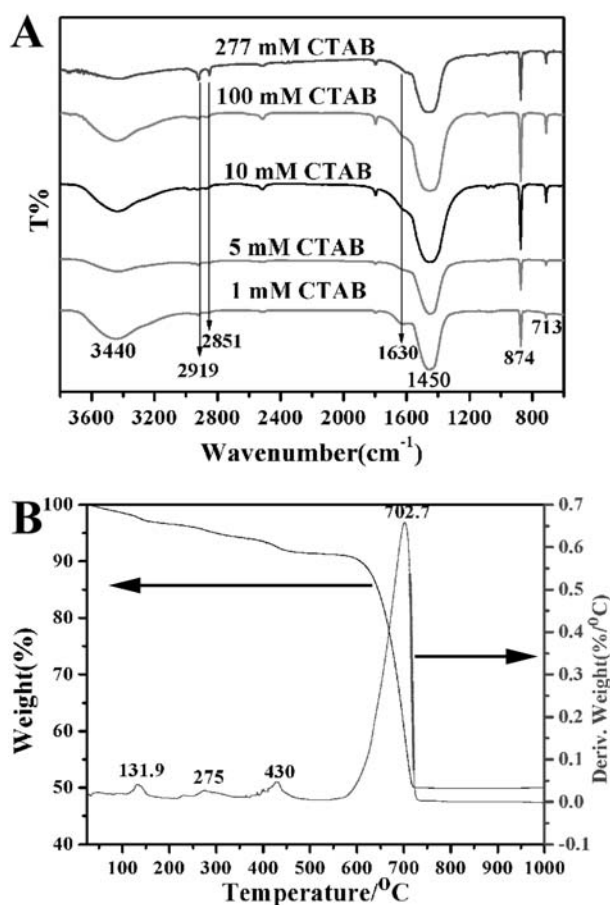


Fig. 2 (A) IR spectra of the samples obtained at various CTAB concentrations after 9 h of reaction. (B) TGA trace of the samples obtained at 10 mM of CTAB after 9 h of reaction.

Clearly, the H^+ ion in citric acid has been replaced with Ca^{2+} , because of the absence of carboxylic acid stretch band characterized by the generally absorption at $1750\text{--}1700\text{ cm}^{-1}$ and the appearance of the antisymmetric stretch band of the carboxylate ion (COO^-) at $1650\text{--}1510\text{ cm}^{-1}$.⁴⁵ The non-symmetrical and symmetrical stretching vibrations of C–H (CH_2) of CTAB are also manifest at 2918 and 2851 cm^{-1} , respectively. The broad peaks around 3440 cm^{-1} should be ascribed to the stretching vibration of O–H from citric acid and water. Therefore, the IR spectra have ascertained that the reaction products contain not only calcite but also CTAB and citric acid molecules. This was confirmed further and quantified to a certain extent by TGA analysis of five samples formed at 1, 5, 10, 100, and 277 mM of CTAB. Since the TGA traces are nearly identical, only the result

Table 1 TGA-determined compositions (wt%) of the samples obtained at various CTAB concentrations (mM) after 9 h of reaction

CTAB concentration	H_2O	Organic matrix	CaCO_3
1	3.57	3.62	92.81
5	3.15	3.36	93.49
10	3.42	3.40	93.18
100	1.05	3.36	95.59
277	1.96	3.28	94.76

of 10 mM CTAB is displayed in Fig. 2B. Several features can be recognized: (i) free and bound water molecules are fully lost at $< 200\text{ }^\circ\text{C}$; (ii) in the temperature range between 200 and $350\text{ }^\circ\text{C}$, the organic matrix has decomposed, and combustion of organic residues occurs at temperatures between 350 and $550\text{ }^\circ\text{C}$ ^{46,47} and (iii) calcium carbonate crystals begin to decompose at $> 550\text{ }^\circ\text{C}$. In this way, the TGA result determined the content (wt%) of the organic matrix (including both CTAB and citric acid) to be 3.62%, 3.36%, 3.40%, 3.36%, and 3.28% in the samples formed at 1, 5, 10, 100, and 277 mM of CTAB, respectively, as shown in Table 1.

We next focus on the crystallization processes that have led to the formation of the complex suite of calcium carbonate crystal morphologies shown in Fig. 1. Firstly, the crystallization started from an amorphous calcium carbonate precursor, as proven by TEM images shown in Fig. 3. The pH of the initial reaction solution was ~ 4.5 . After exposing the solution to a NH_4HCO_3 atmosphere for 4.5 h, the mother solution started to become turbid, as can be clearly seen from ESI Fig. SI-2A,† and at the same time, the pH increased to ~ 9.4 . The corresponding TEM image (Fig. 3B) shows amorphous particles in a size range of 3–10 nm sampled from the mother solution, which gives no lattice fringes and diffraction spots were not detected in the SAED pattern (inset of Fig. 3B). Larger particles 100–150 nm in diameter can also be found in the sample (Fig. 3C), which is still in an amorphous phase (see the SAED pattern in the inset of Fig. 3C), presumably resulting from aggregation and growth of the smaller ACC particles (perhaps even smaller than 3 nm) via the Ostwald ripening process. Finally, we checked the elemental composition of the amorphous nanoparticles by acquiring the EDX pattern (ESI, Fig. SI-2B),† confirming that the amorphous nanoparticles are indeed made of calcium carbonate. In addition, the Raman spectrum of the particles shown in Fig. 3D exhibits only a major but rather broad peak at $\sim 1085\text{ cm}^{-1}$ in contrast to the sharp peaks normally seen in crystalline forms of calcium carbonate, but in conformity with that of ACC.^{48,49} It is noted

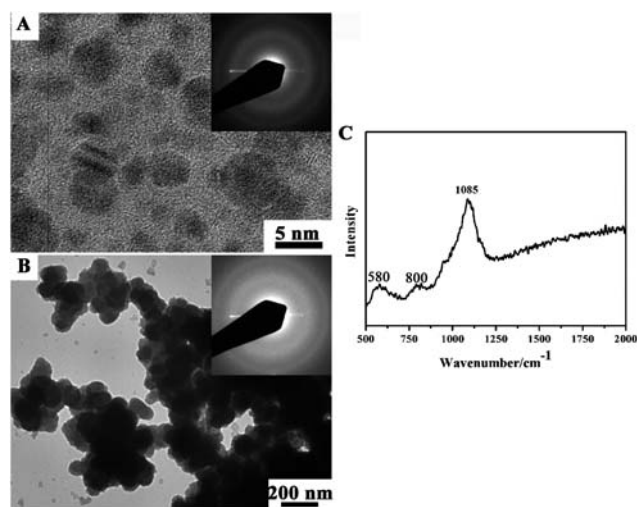


Fig. 3 (A, B) TEM images of the samples obtained after 4.5 h of reaction in the atmosphere of NH_4HCO_3 (insets: the corresponding SAED patterns). (C) Raman spectrum of the particles formed after 4.5 h of reaction in the atmosphere of NH_4HCO_3 .

that Tlini *et al.* reported the ν_1 symmetric stretching of carbonate ion of ACC to be at 1077 cm^{-1} .⁵⁰ Such a shift of the carbonate ion stretching band may be due to the different ACC forming condition, such as the reaction temperature. The broad peaks at ~ 580 and $\sim 800\text{ cm}^{-1}$ may be ascribed, respectively, to the skeletal (*e.g.*, C–C–C and C_3CO) deformations of citric acid. It thus appears that the small ACC nanoparticles in a size range of 3–10 nm were initially nucleated from the mother solution, and then aggregated and grown into larger ACC particles in a diameter range of 100–150 nm. This is in step with the template-directed mineralization of CaCO_3 under a stearic acid monolayer reported recently by Pouget *et al.*,²¹ which consisted of nucleation of ~ 30 nm amorphous nanoparticles from a supersaturated calcium bicarbonate solution *via* aggregation of 0.6–1.1 nm pre-nucleation clusters and aggregation/growth into larger amorphous particles with sizes ranging from 70 to 120 nm. Such

a crystallization process clearly differs from the classical crystallization whereby the nucleation clusters grow after they reach a critical size, finally forming single crystals *via* addition of ions/molecules.

To gain a deeper understanding of the crystallization processes at various CTAB concentrations, the samples were collected at different stages of the reaction and observed by SEM. Representative SEM snapshots of the products obtained at different conditions are serially shown in Fig. 4. First and foremost, an overall trend from spherical particles on the top-left to more anisotropic superstructures on the bottom-right is striking with the increase of the CTAB concentration and/or the reaction time. After 1 h of reaction, spherical particles (~ 300 – 400 nm) composed of nanoparticles ~ 10 nm in diameter were formed at 1, 5, 10 and 100 mM CTAB (Fig. 4A–D) with a heightened degree of aggregation. When [CTAB] was 277 mM, rod-shaped calcium

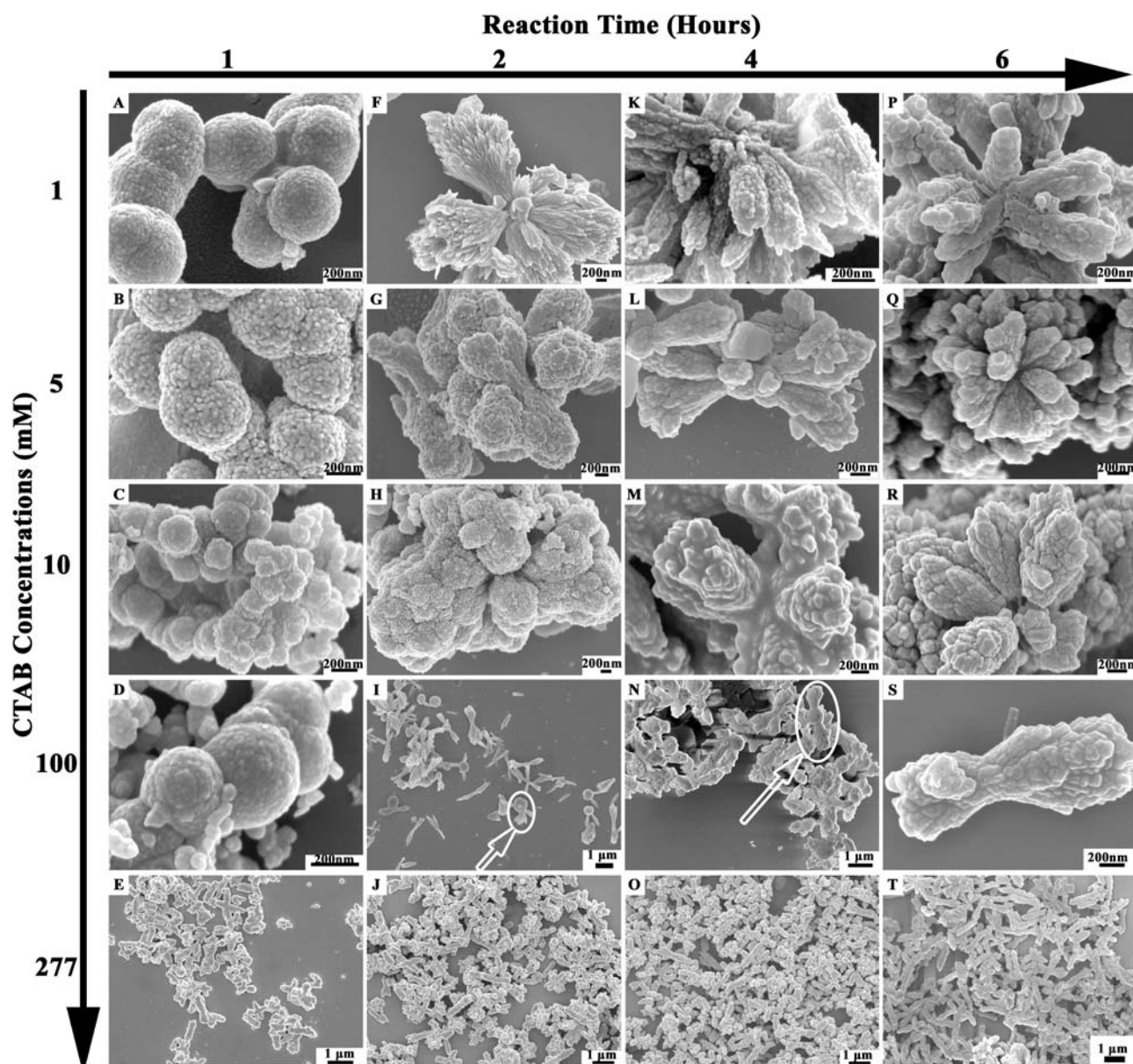


Fig. 4 SEM images of the samples collected from different reaction stages at 1, 5, 10, 100, and 277 mM CTAB.

carbonate crystals were formed, and this morphology almost remained unchanged even with the prolonging of the reaction time (see Fig. 4E, 4J, 4O and 4T). In addition, from the pH drift assay *vs.* reaction time (ESI, Fig. SI-3),[†] we find that the extent of decline in pH increased with the increase of CTAB concentration. The continuous decline of pH with the reaction time arose from the crystallization of calcium carbonate: $\text{Ca}^{2+} + \text{HCO}_3^- \rightarrow \text{CaCO}_3 + \text{H}^+$. One can thus conclude that the higher the CTAB concentration is, the faster the crystallization rate is. This is the reason why the final rod-shaped calcium carbonate crystals are formed after only 1 h of reaction at 277 mM CTAB. With the reaction time prolonging to 2 h, surrounding the spherical particle aggregates in the cores cluster-like branches emerged and radiated along all directions at 1, 5, and 10 mM CTAB (Fig. 4F–H). These branches are composed of nanoparticles about 10 nm in a diameter, as seen from the corresponding high magnification SEM images (ESI, Fig. SI-3A–D).[†] At 100 mM CTAB, the spherical particles are also present as the core, and the peripheral has developed into spiciform-like branches (Fig. 4I and ESI, Fig. SI-3E).[†] These spiciform-shaped branches are composed of short-rod shaped particles (ESI, Fig. SI-3F).[†] With a reaction time of 4 h, the radiating cluster-shaped branches gradually retreated from each other at 1, 5, and 10 mM CTAB (Fig. 4 K–M). The spiciform shaped branches got bigger at 100 mM CTAB, which mainly grew on the opposite sides of the spherical core (like a sheaf), as can be seen from the white circle in Fig. 4N. When the reaction time was further extended to 6 h, the crystallization degree of the branches formed at 1, 5, 10, and 100 mM CTAB was further increased, forming the crystals nearly as the same as that formed after 9 h of reaction (Fig. 4P–S). The result above can be summarized as follows: (i) at 1, 5 and 10 mM CTAB, the crystallization processes are almost the same. Spherical-shaped particles are firstly formed from the mother solution, and their aggregations gradually evolve into cluster-like branches radiating along all directions. These branches continue to segregate and crystallize with the increase of reaction time; (ii) at 100 mM CTAB, the spherical-like particles are also firstly precipitated from the mother solution, but their competing aggregation and segregation lead to the branching development on the opposite sides, forming the spiciform-like branches composed of short rod-shaped particles. These branches continuously grow and crystallize to form the final sheaf-like crystals; and (iii) the higher CTAB concentration gives rise to faster reactions. The CTAB micelles were attracted to the aggregates of citric acid stabilized amorphous calcium carbonate to template the crystallization. The crystallization rate was so high at 277 mM CTAB that the final rod-shaped crystals had formed from the mother solution after only 1 h of reaction, as revealed by the profiles of the pH drift assay *vs.* reaction time.

Although the SEM results have provided the essential information for the general morphological evolution in the crystallization processes, they normally fall short of divulging the internal structural details, *e.g.*, the degree of crystallization, of the samples in question. Therefore, we turned to TEM observations. Because the crystallization processes are almost the same at 1, 5, and 10 mM CTAB, TEM analysis of the samples formed at 10 mM CTAB in Fig. 5 is reported here as an example. After 1 h of reaction, the formed spherical-shaped particles with sizes of 300–400 nm are still in an amorphous phase (Fig. 5A), which

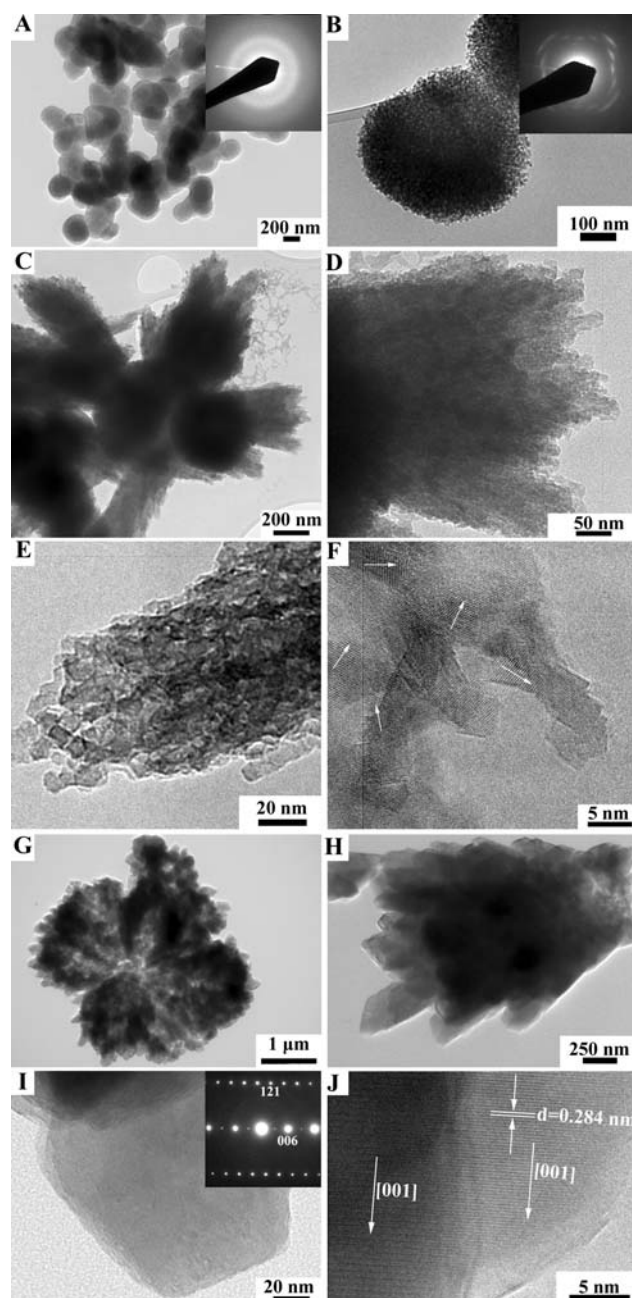


Fig. 5 TEM images of calcium carbonate crystals formed at different reaction stages in the presence of 10 mM CTAB: (A) spherical particles formed after 1 h of reaction and the corresponding SAED pattern (inset); (B) spherical particles formed after 2 h of reaction and the corresponding SAED pattern (inset); (C) cluster-like branches radiating from the aggregated spherical particles collected after 2 h of reaction; (D, E) high magnification TEM and (F) HRTEM images of the radiating cluster-like branches; (G) a sample collected after 9 h of reaction; (H, I) high magnification TEM images and corresponding SAED pattern (inset of Figure S1); (J) HRTEM image corresponding to (G).

can be clearly seen from the corresponding SAED pattern (inset of Fig. 5A). With the reaction time increasing to 2 h, the amorphous spherical particles were gradually transformed into spherical polycrystalline calcite particles (Fig. 5B) together with the surrounding radiating cluster-like branches (Fig. 5C), driven

by aggregation. From the high magnification TEM images in Fig. 5D and E, we find that the branches are composed of polycrystalline small spherical nanoparticles, as clearly seen from the HRTEM images (Fig. 5F), in accordance with the SEM results. When the reaction time was prolonged to 9 h, the aggregated spherical particles in the core disappeared (Fig. 5G). The cluster-like branches radiating from the core became clearly different (Fig. 5H) from those formed after 2 h of reaction (Fig. 5D) in that they are composed of large faceted crystal grains instead of small spherical nanoparticles (Fig. 5I). These large faceted crystal grains take a single crystal structure according to the corresponding SAED pattern (inset of Fig. 5I) and the HRTEM image (Fig. 5J).

Fig. 6 shows TEM images of the samples formed at different reaction stages in the presence of 100 mM CTAB. When the reaction time was 2 h, polycrystalline calcite particles with spherical cores 300–400 nm in size were formed (Fig. 6A) from spherical amorphous particles in much the same way as in the transformation process in the presence of 10 mM CTAB (Fig. 5A, B). The spiciform shaped branches are grown from the polycrystalline spherical cores (Fig. 6A), and composed of short rod-shaped particles about 10 nm in diameter (Fig. 6B). The polycrystalline structure is reflected in the corresponding SAED pattern (inset of Fig. 6A) and HRTEM image, with the latter revealing both amorphous (black circles in Fig. 6C) and crystalline (white arrows in Fig. 6C) particles in the superstructure. When the reaction time was increased to 4 h, the spiciform shaped branches continuously grew and the crystal grains

gradually expanded as seen from the TEM image (Fig. 6D) and the corresponding HRTEM image (Fig. 6E). Other than that, the spherical cores, still polycrystalline (see Fig. 6F), are not much different in morphology from the spherical particles formed after 2 h of reaction (Fig. 6A). With the reaction time further prolonging to 9 h, crystals with the sheaf morphology were formed, accompanied by the disappearance of the spherical cores (Fig. 6G) in accordance with the SEM result (Fig. 1D). Notice that the crystal grains become larger (Fig. 6H) and gradually develop into single crystals (Fig. 6I).

We finally present TEM images of the samples collected at various reaction stages in the presence of 277 mM CTAB in Fig. 7. Here even when the reaction time was cut to 20 min, bundles of short rod-shaped particles have already formed (Fig. 7A and B). The short rod-shaped particles about 20 nm in diameter have a hollow structure, as seen from the corresponding HRTEM images (see arrow in Fig. 7C). The bundles of smaller rods were crystallized into larger rods as the reaction time was prolonged to 1 h (Fig. 7D), which are also hollow as can be seen from the high magnification SEM image (see arrow in Fig. 7E), and are composed of polycrystalline particles (Fig. 7F). With a further increase of reaction time to 9 h, the morphologies did not change much (Fig. 7G), but the crystal grains in the rod-shaped particles continually grew in size (Fig. 7H) and eventually crystallized into larger single crystals, as shown in the corresponding SAED pattern (inset of Fig. 7H) and HRTEM image (Fig. 7I). From the HRTEM images obtained at various CTAB concentrations and reaction stages (Fig. 5F → 5J, Fig. 6C → 6E

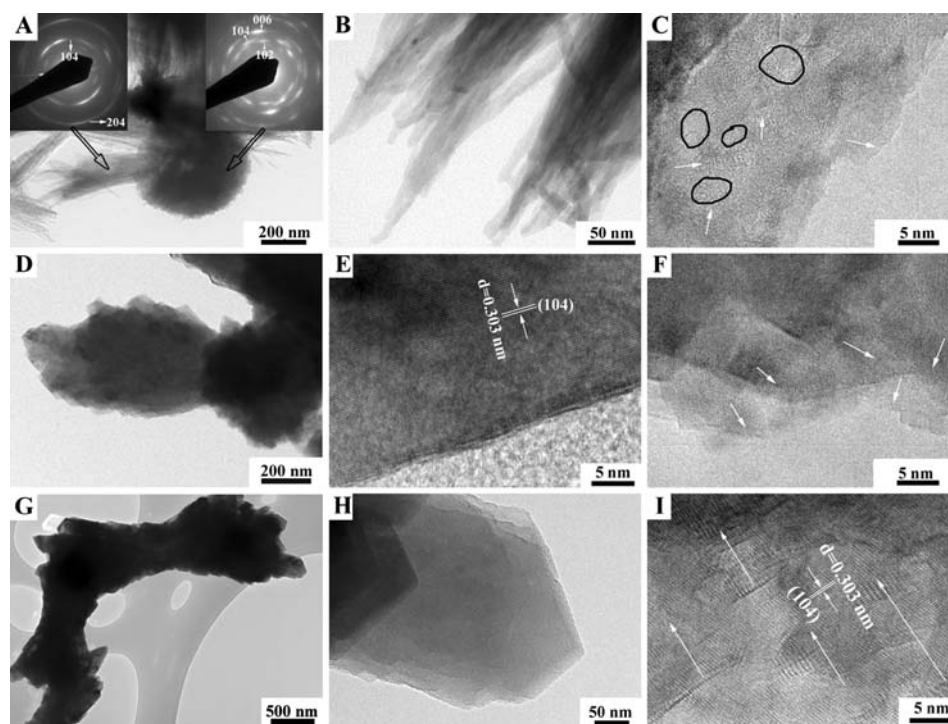


Fig. 6 TEM images of the samples formed at different reaction stages in the presence of 100 mM CTAB: (A) a spherical core and the radiating spiciform shaped branches collected after 2 h of reaction (inset shows the corresponding SAED patterns); (B, C) high magnification TEM and HRTEM images of the spiciform shaped branches; (D) spherical cores and the radiating spiciform shaped branches collected after 4 h of reaction; (E) HRTEM image of the spiciform shaped branches corresponding to (D); (F) HRTEM image of the spherical cores corresponding to (D); (G) sheaf-like crystals collected after 9 h of reaction; (H, I) high magnification TEM and HRTEM images corresponding to (G).

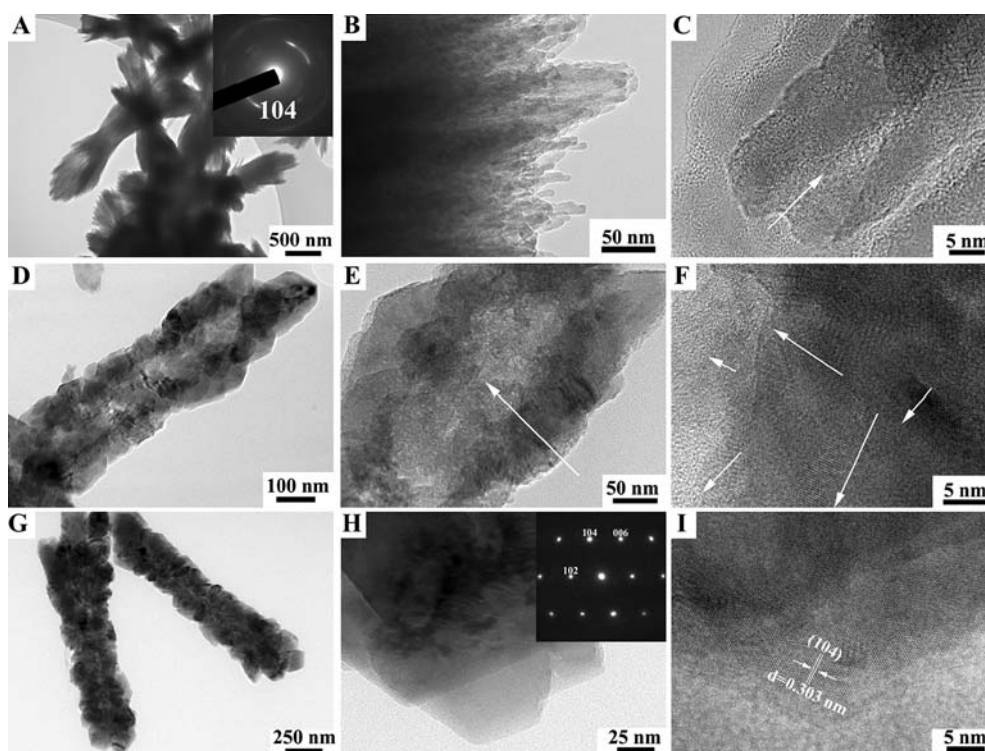


Fig. 7 TEM images of the samples collected at various reaction stages in the presence of 277 mM CTAB: (A–C) bundles of rods collected after 20 min of reaction and the corresponding SAED pattern (inset), high magnification TEM image and HRTEM image; (D–F) rod-shaped crystals formed after 1 h of reaction and the corresponding high magnification TEM image and HRTEM image; (G–I) rod-shaped crystals formed after 9 h of reaction and the corresponding high magnification TEM image, SAED pattern (inset) and HRTEM image.

→ 6I, Fig. 7F → 7I), we can find that the crystallographic directions of the nanocrystals gradually line up and the ensemble is transformed from disorder by fusing the nanocrystals together to form continuous lattice fringes. Such a transformation from the most unstable amorphous phase to the most stable calcite phase is in line with the Ostwald–Volmer rule. In a nutshell, our kinetic study by TEM has revealed that amorphous particles were firstly nucleated and gradually crystallized into small nanocrystals, which were then fused into larger polycrystals with the elapse of reaction time.

Although details of the crystallization process here can be complex, the general mechanism has emerged for the morphological evolution of calcium carbonate crystals at various CTAB concentrations on the basis of the results presented above. During the period of exposure to the NH_4HCO_3 atmosphere, the pH and supersaturation of the mother solution gradually increased due to the continuous uptake of NH_3 and CO_2 . Once a certain level of supersaturation was reached after 4.5 h, calcium carbonate was initially nucleated from the mother solution to form amorphous nanoparticles 3–10 nm in diameter (Fig. 8A). These amorphous nanoparticles have relatively high surface energy and thus prone to aggregation to reduce surface energy, growing into larger amorphous particles in a diameter range of 100–150 nm (Fig. 8B). According to the IR result, the carboxyl groups of citric acid were ionized to form carboxylate ions after 4.5 h storage in the NH_4HCO_3 atmosphere because the pH value of the solution (9.4 or so) was larger than the pK_a values ($\text{pK}_1 = 3.13$, $\text{pK}_2 = 4.76$, $\text{pK}_3 = 6.40$).⁵¹ It was previously reported that citric acid molecules have no influence on the

nucleation of CaCO_3 but can inhibit its growth due to the stronger affinity of citric acid for CaCO_3 particles than for free Ca^{2+} ions in solution.⁵¹ We therefore believe that the citric acid molecules in our case were adsorbed on the ACC particles *via* ion pair interactions between COO^- and Ca^{2+} , which is supported by the our zeta potential data (−26.4 mV). When positively charged CTAB molecules were added, they adsorbed preferentially on the negative charged surfaces of the amorphous particles *via* electrostatic interaction, as revealed by the zeta potential change of these particles from negative (−26.4 mV) to positive (23.2, 26.7, 26.9, 31.8, and 37.7 mV at 1, 5, 10, 100, and 277 mM CTAB, respectively). As a result, the amorphous particles self-assemble to form various structures depending on CTAB concentrations driven by the hydrophobic interactions among the hydrocarbon chains of the CTAB molecules. The higher the CTAB concentration is, the higher supersaturation degree of $[\text{CaCO}_3]$ will be around the CTAB micellar structure. Consequently, the crystallization rate will increase with the increasing CTAB concentration, as revealed from the results of SEM and pH drift assay *vs.* reaction time (Fig. 4 and ESI, Fig. SI-3).[†] This, in turn, has triggered the following morphological evolution accompanied by crystallization.

(i) At 1, 5, and 10 mM CTAB, with the increase of reaction time, the amorphous particles (~100–150 nm), capped by CTAB molecules *via* the electrostatic attraction between the positively charged groups of CTAB and the negatively charged carboxyl groups of citric acid, continued to grow, forming larger ACC particles in the size range of 300–400 nm (Fig. 8C). Such growth was fed by the neighbouring ACC nanoparticles accrued *via* the

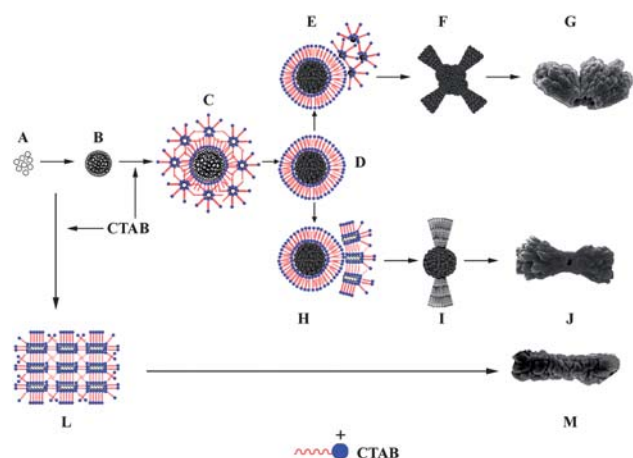


Fig. 8 Schematic representation of the formation mechanism of calcium carbonate from citric acid stabilized amorphous calcium carbonate at various CTAB concentrations: (A) amorphous calcium carbonate nuclei 3–10 nm in diameter were initially nucleated in the mother solution, (B) the ACC nuclei then aggregated and grew into larger amorphous particles with a size of 100–150 nm; (C) addition of CTAB molecules triggered further aggregation of the amorphous particles into the size range of 300–400 nm, (D) and gradually transformed into polycrystalline particles with the reaction time prolonging; (E) at 1, 5, and 10 mM CTAB, calcium carbonate nuclei 10 nm across were formed at the surfaces of these spherical polycrystalline cores, and further assembled into radiating cluster-like branches along all directions (F), and (G) finally crystallized into hollow radiating cluster-like branches; (H) at 100 mM CTAB, short rod-shaped nanoparticles ~ 10 nm in diameter were nucleated at the surfaces of the polycrystalline spherical cores from step (D), and then assembled into spiciform shaped branches on the opposite sides to form a sheaf-like structure (I), and (J) finally formed into hollow crystals with a sheaf-like morphology; (L) at 277 mM CTAB, short rod-shaped nanoparticle ~ 20 nm in diameter directly formed from amorphous precursors (step A and B) were assembled into the bundled crystals, and (M) transformed into hollow rod-shaped crystals.

hydrophobic interaction between the CTAB molecules. The amorphous particles thus formed were unstable, so gradually transformed into particles with randomly oriented nanocrystalline domains in an evolving dynamic equilibrium with the remaining amorphous domains, and finally into polycrystalline particles with a similar size of approximately 300–400 nm (Fig. 8D). Such polycrystalline spherical particles appear to act as nucleation sites to take in new calcium carbonate onto the surfaces. It is well known that CTAB molecules in water self-assemble into spherical micelles above its critical micellization concentration (CMC) of ~ 1 mM and below 10 times this CMC at room temperature. Therefore, at 1, 5, and 10 mM CTAB, the newly formed calcium carbonate nuclei are spherical due to the template effect of spherical CTAB micelles (Fig. 8E). With the prolonging of reaction time, the spherical calcium carbonate nuclei ~ 10 nm in diameter were continuously formed on the surfaces of the spherical core particles to form the radiating cluster-like branches (Fig. 8F) effected by the template effect of spherical CTAB micelles. The calcium carbonate branches grew continuously on the surfaces of the spherical cores at the cost of their vicinal CaCO_3 particles due to Ostwald-ripening. This may be enhanced by the surfactant induced segregation because the spherical cores prefer association with each other to lower

surface energy in the absence of CTAB, but the addition of CTAB tends to turn the spherical cores away from each other due to the reduced surface energy. Eventually, only a few large separated branches could continue the growth at the cost of the spherical shaped cores and the nanoparticles in the interior of the radiating cluster-like branches (Fig. 8G), which can also be seen from Figure SI-5, akin to those observed by Colfen *et al.*^{52,53} Therefore, in the crystals finally formed, the spherical shaped cores have dissolved and the radiating cluster-like branches take a hollow structure. To recap, the crystallization process at 1, 5, 10 mM CTAB would follow the (A \rightarrow B \rightarrow C \rightarrow D \rightarrow E \rightarrow F \rightarrow G) pathway.

(ii) At 100 mM CTAB, the polycrystalline spherical cores acted as the nucleation sites for the deposition of new short rod-shaped calcium carbonate particles due to the template effect of rod-shaped CTAB micelles. The short rod-shaped calcium carbonate nuclei were further assembled into the spiciform shaped branches, developing into a sheaf-like structure due to Ostwald-ripening and particle segregation arising from the CTAB-induced lowering of surface energy and electrostatic repulsion. With the reaction time prolonging, the crystal grains at the exterior of the spiciform shaped branches tended to grow into larger single crystals at the cost of the spherical cores and the short rod-shaped particles at the interior of the spiciform shaped branches to form the hollow structure. Thus, the crystallization process at 100 mM CTAB would go along the (A \rightarrow B \rightarrow C \rightarrow D \rightarrow H \rightarrow I \rightarrow J) pathway.

(iii) Finally, at 277 mM CTAB, short rod-shaped particles were rapidly nucleated under the template effect of CTAB micelles directly from the ACC particles, which then formed well aligned bundles *via* hydrophobic interactions. With the reaction time prolonging, the short rod-shaped particles on the exterior of the bundles grew into larger crystal grains at the cost of the particles in the interior, forming a hollow rod shaped structure. This is designated as the (A \rightarrow B \rightarrow L \rightarrow M) pathway.

Conclusions

As a summary, the crystallization processes of calcium carbonate at various CTAB concentrations have been studied, starting from a mother solution containing an amorphous calcium carbonate precursor stabilized by citric acid molecules, which point to non-classical crystallization pathways similar to biomineralization in organisms. The commonality of the non-classical crystallization pathways is that they all start from an amorphous calcium carbonate precursor stabilized by carboxylic acid molecules, analogous to amorphous phase stabilized by acidic proteins in organisms, and thus may shed light on important biomineralization processes. The formed crystals show interesting morphologies (hollow radiating cluster-like particles, hollow sheaf-like crystals, hollow rod-shaped crystals) which are regulated by CTAB concentration and are polycrystalline. These morphologies are completely different from those normally formed by the direct mixing of Ca^{2+} and CO_3^{2-} , in which the nucleation rate is very fast due to the instantaneous high supersaturation and the conventional rhombohedral calcite crystals are always formed ultimately no matter with or without CTAB. Similarly, citric acid molecules alone have little influence on the final morphology and structure of CaCO_3 either, apart

from just hindering the mineral growth. However, our study has shown that the organic matrix of CTAB, despite its weak interaction with calcium and carbonate ions, could still control the morphology of calcium carbonate *via* non-classical crystallization processes by starting from citric acid stabilized amorphous particles. Therefore, this method would allow us to pragmatically realize the kind of morphological control of biomineralization and should be useful for synthesizing hollow calcium carbonate crystals among others, which might find use in drug delivery and biomedical areas.

Acknowledgements

This work was supported by the Hong Kong Research Grants Council General Research Funds, GRF No. HKUST 604107.

References

- 1 H. A. Lowenstam and S. Weiner, *On Biomineralization*, Oxford University press, New York, 1989.
- 2 B. L. Smith, T. E. Schaffer, M. Viani, J. B. Thompson, N. A. Frederick, J. Kindt, A. Belcher, G. D. Stucky, D. E. Morse and P. K. Hansma, *Nature*, 1999, **399**, 761.
- 3 J. Aizenberg, J. C. Weaver, M. S. Thanawala, V. C. Sundar, D. E. Morse and P. Fratzl, *Science*, 2005, **309**, 275.
- 4 D. D. Archibald and S. Mann, *Nature*, 1993, **364**, 430.
- 5 S. Mann and G. A. Ozin, *Nature*, 1996, **382**, 313.
- 6 C. P. Gibson and K. J. Putzer, *Science*, 1995, **267**, 1338.
- 7 T. S. Ahmadi, Z. L. Wang, T. C. Green, A. Henglein and M. A. ElSayed, *Science*, 1996, **272**, 1924.
- 8 H. Yang, N. Coombs and G. A. Ozin, *Nature*, 1997, **386**, 692.
- 9 M. Li, H. Schnablegger and S. Mann, *Nature*, 1999, **402**, 393.
- 10 X. G. Peng, L. Manna, W. D. Yang, J. Wickham, E. Scher, A. Kadavanich and A. P. Alivisatos, *Nature*, 2000, **404**, 59.
- 11 L. J. Bonderer, A. R. Studart and L. J. Gauckler, *Science*, 2008, **319**, 1069.
- 12 E. Munch, M. E. Launey, D. H. Alsem, E. Saiz, A. P. Tomsia and R. O. Ritchie, *Science*, 2008, **322**, 1516.
- 13 H. Colfen and S. Mann, *Angew. Chem., Int. Ed.*, 2003, **42**, 2350.
- 14 F. C. Meldrum and H. Colfen, *Chem. Rev.*, 2008, **108**, 4332.
- 15 N. A. J. M. Sommerdijk and G. de With, *Chem. Rev.*, 2008, **108**, 4499.
- 16 L. B. Gower, *Chem. Rev.*, 2008, **108**, 4551.
- 17 H. Colfen, *Top. Curr. Chem.*, 2007, **271**, 1.
- 18 S. H. Yu, *Top. Curr. Chem.*, 2007, **271**, 79.
- 19 Y. J. Chen, J. W. Xiao, Z. N. Wang and S. H. Yang, *Langmuir*, 2009, **25**, 1054.
- 20 J. W. Xiao, Z. N. Wang, Y. C. Tang and S. H. Yang, *Langmuir*, 2010, **26**, 4977.
- 21 E. M. Pouget, P. H. H. Bomans, J. A. C. M. Goos, P. M. Frederik, G. de With and N. A. J. M. Sommerdijk, *Science*, 2009, **323**, 1455.
- 22 A. M. Belcher, X. H. Wu, R. J. Christensen, P. K. Hansma, G. D. Stucky and D. E. Morse, *Nature*, 1996, **381**, 56.
- 23 S. Raz, S. Weiner and L. Addadi, *Adv. Mater.*, 2000, **12**, 38.
- 24 D. B. DeOliveira and R. A. Laursen, *J. Am. Chem. Soc.*, 1997, **119**, 10627.
- 25 C. M. Li, G. D. Botsaris and D. L. Kaplan, *Cryst. Growth Des.*, 2002, **2**, 387.
- 26 J. W. Xiao, Y. C. Zhu, Y. Y. Liu, H. J. Liu, Y. Zeng, F. F. Xu and L. Z. Wang, *Cryst. Growth Des.*, 2008, **8**, 2887.
- 27 S. H. Yu and H. Colfen, *J. Mater. Chem.*, 2004, **14**, 2124.
- 28 S. F. Chen, S. H. Yu, T. X. Wang, J. Jiang, H. Colfen, B. Hu and B. Yu, *Adv. Mater.*, 2005, **17**, 1461.
- 29 Y. X. Gao, S. H. Yu, H. P. Cong, J. Jiang, A. W. Xu, W. F. Dong and H. Colfen, *J. Phys. Chem. B*, 2006, **110**, 6432.
- 30 R. Q. Song, H. Colfen, A. W. Xu, J. Hartmann and M. Antonietti, *ACS Nano*, 2009, **3**, 1966.
- 31 R. Q. Song, A. W. Xu, M. Antonietti and H. Colfen, *Angew. Chem., Int. Ed.*, 2009, **48**, 395.
- 32 J. J. J. M. Donners, R. J. M. Nolte and N. A. J. M. Sommerdijk, *J. Am. Chem. Soc.*, 2002, **124**, 9700.
- 33 S. B. Mukkamala and A. K. Powell, *Chem. Commun.*, 2004, 918.
- 34 K. Naka, Y. Tanaka, Y. Chujo and Y. Ito, *Chem. Commun.*, 1999, 1931.
- 35 K. Naka, Y. Tanaka and Y. Chujo, *Langmuir*, 2002, **18**, 3655.
- 36 L. A. Estroff, C. D. Incavito and A. D. Hamilton, *J. Am. Chem. Soc.*, 2004, **126**, 2.
- 37 M. Lei, P. G. Li, Z. B. Sun and W. H. Tang, *Mater. Lett.*, 2006, **60**, 1261.
- 38 J. G. Yu, X. F. Zhao, B. Cheng and Q. J. Zhang, *J. Solid State Chem.*, 2005, **178**, 861.
- 39 L. M. Qi, J. Li and J. M. Ma, *Adv. Mater.*, 2002, **14**, 300.
- 40 Y. C. Zhu, Y. Y. Liu, Q. C. Ruan, Y. Zeng, J. W. Xiao, Z. W. Liu, L. F. Cheng, F. F. Xu and L. L. Zhang, *J. Phys. Chem. C*, 2009, **113**, 6584.
- 41 S. Weiner, *J. Exp. Zool.*, 1985, **234**, 7.
- 42 S. C. Benson, N. C. Benson and F. Wilt, *J. Cell Biol.*, 1986, **102**, 1878.
- 43 J. G. Yu, M. Lei, B. Cheng and X. J. Zhao, *J. Cryst. Growth*, 2004, **261**, 566.
- 44 F. A. Andersen and L. Brecevic, *Acta Chem. Scand.*, 1991, **45**, 1018.
- 45 G. Socrates, *Infrared and Raman Characteristic Group Frequencies, Tables and Charts*, John Wiley and sons, 2001.
- 46 X. H. Liu, X. H. Luo, S. X. Lu, J. C. Zhang and W. L. Cao, *J. Colloid Interface Sci.*, 2007, **307**, 94.
- 47 H. Cheng, L. P. Wang and Z. G. Lu, *Nanotechnology*, 2008, **19**, DOI: 10.1088/0957-4484/19/02/025706.
- 48 L. Addadi, S. Raz and S. Weiner, *Adv. Mater.*, 2003, **15**, 959.
- 49 Y. Oaki, S. Kajiyama, T. Nishimura, H. Imai and T. Kato, *Adv. Mater.*, 2008, **20**, 3633.
- 50 M. M. Tlili, M. Ben Amor, C. Gabrielli, S. Joiret, G. Maurin and P. Rousseau, *J. Raman Spectrosc.*, 2002, **33**, 10.
- 51 N. Wada, K. Kanamura and T. Umegaki, *J. Colloid Interface Sci.*, 2001, **233**, 65.
- 52 H. Colfen and M. Antonietti, *Langmuir*, 1998, **14**, 582.
- 53 S. H. Yu, H. Colfen and M. Antonietti, *J. Phys. Chem. B*, 2003, **107**, 7396.